

Article

Development of a High Sampling Rate Data Acquisition System Working in a High Pulse Count Rate Region for Radiation Diagnostics in Nuclear Fusion Plasma Research

Kunihiro Ogawa ^{1,2,*}, Siriyaporn Sangaroon ³, Long Yong Liao ⁴, Eiji Takada ⁵ and Mitsutaka Isobe ^{1,2}

- ¹ National Institute for Fusion Science, 322-6 Oroshi-cho, Toki 509-5202, Japan; isobe.mitsutaka@nifs.ac.jp
² Fusion Science Program, The Graduate University for Advanced Studies, SOKENDAI, 322-6 Oroshi-cho, Toki 509-5202, Japan
³ Department of Physics, Mahasarakham University, Maha Sarakham 44150, Thailand; siriyaporn.s@msu.ac.th
⁴ Department of Fusion Science, The Graduate University for Advanced Studies, SOKENDAI, 322-6 Oroshi-cho, Toki 509-5202, Japan; liao.longyong@nifs.ac.jp
⁵ National Institute of Technology, Gakujutsu-Sogo-Center 10F, 2-1-1 Hitotsubashi, Chiyoda-ku 101-0003, Japan; e_takada@kosen-k.go.jp
* Correspondence: ogawa.kunihiro@nifs.ac.jp; Tel.: +81-572-58-2229

Abstract: In this study, a high sampling rate data acquisition system with the ability to provide timestamp, pulse shape information, and waveform simultaneously under a sub megahertz pulse counting rate was developed for radiation diagnostics for magnetic confinement nuclear fusion plasma research. The testing of the data acquisition system under the high pulse counting rate condition using real signals was performed in an accelerator-based deuterium-deuterium fusion neutron source (Fast Neutron Source) at the Japan Atomic Energy Agency. We found that the pulse counts acquired by the system linearly increased up to 6×10^5 cps, and the count loss at 10^6 cps was estimated to be ~10%. The data acquisition system was applied to deuterium-deuterium neutron profile diagnostics in the deuterium gas operation of a helical-type magnetic confinement plasma device, called the Large Helical Device, to observe the radial profile of neutron emissivity for the first time in a three-dimensional magnetic confinement fusion device. Time-resolved measurements of the deuterium-deuterium fusion emission profile were performed. The experimentally observed radial neutron emission profile was consistent with numerical predictions based on the orbit-following models using experimental data. The data acquisition system was shown to have the desired performance.

Keywords: radiation measurement; data acquisition; high sampling rate; fusion plasma; high pulse count rate; pulse shape analysis; pulse height analysis; waveform storage



Citation: Ogawa, K.; Sangaroon, S.; Liao, L.Y.; Takada, E.; Isobe, M. Development of a High Sampling Rate Data Acquisition System Working in a High Pulse Count Rate Region for Radiation Diagnostics in Nuclear Fusion Plasma Research. *Electronics* **2023**, *12*, 3898. <https://doi.org/10.3390/electronics12183898>

Academic Editors: Alberto Fernandez Hilario and Simeone Marino

Received: 8 August 2023
Revised: 8 September 2023
Accepted: 14 September 2023
Published: 15 September 2023



Copyright: © 2023 by the authors. Licensee MDPI, Basel, Switzerland. This article is an open access article distributed under the terms and conditions of the Creative Commons Attribution (CC BY) license (<https://creativecommons.org/licenses/by/4.0/>).

1. Introduction

One of the attractive solutions for the global energy crisis is the attainment of an ultimate energy source, i.e., magnetic confinement nuclear fusion [1]. Currently, the construction of ITER is progressing as an international joint project, and several startup companies propose to build fusion reactors [2]. We are now facing the start of the nuclear burning plasma era. The development of radiation detectors for fusion research has been undertaken because radiation diagnostics will be utilized as the fusion power monitor in a fusion reactor [3–5]. One of the issues in building fusion reactors is understanding and predicting energetic particle confinement because the future fusion burning plasma in a fusion reactor will be mainly heated by energetic particles [6]. In current research, energetic particles are injected using a neutral beam injector or created by the ion cyclotron range of frequency wave heating [7,8]. Radiation detectors are utilized as energetic particle diagnostic tools because fast neutrons are mainly created by fusion reactions due to energetic particles and bulk ions [9,10]. Additionally, gamma rays are regarded as complementary to fast

neutron diagnostics [11,12] and are utilized as the main diagnostic tools for aneutronic fusion plasma studies [13–15].

One of the critical requirements of radiation detectors for magnetic fusion physics research is high time resolution as well as high energy resolution because a plasma rapidly changes over time. For example, due to energetic-particle-driven magnetohydrodynamic instabilities [16,17], the expulsion of energetic particles was observed in the order of milliseconds or even shorter [18–22]. In pulse count mode, the statistical error of the count is expressed as \sqrt{N} , where N stands for a count. We need sufficient counts in each time bin for the analysis of physics phenomena based on significant observations. Therefore, a high pulse count rate capability is desired for high time-resolved measurements. A scintillation detector with pulse shape discrimination ability has been commonly utilized in fusion research, especially as the neutron energy spectrum measurement [23–27] or neutron emission profile measurement [28–32]. To obtain better performance of neutron and gamma-ray discrimination, data acquisition with a high sampling rate is required [33–35]. Then, a high sampling rate data acquisition system working in the high pulse count rate region has been developed.

One of the most famous companies to develop data acquisition systems for radiation diagnostics is CAEN, Italy [36]. CAEN has manufactured a novel high sampling rate data acquisition system having a pulse shape discrimination ability working in a high pulse count rate region with user-friendly software, e.g., digital pulse processing for charge integration and pulse shape discrimination DPP-PSD [37] using the charge integral method [38]. The data acquisition system simultaneously provides timestamp and pulse shape information, which are essential for radiation diagnostics, with the analyses of pulse height [39], time of flight [40], and pulse shape discrimination [41]. For obtaining better performance of neutron and gamma-ray discrimination, much attention has been paid to the development of new analysis methods in pulse shape discrimination, such as the pulse gradient analysis [42], the zero crossing method [43], and the discrete wavelet transform [44]. Recently, studies of pulse shape discrimination using neural networks [45,46] and recovery of pulse pile-up were performed [47]. Applying those novel methods can provide a better pulse shape discrimination ability which might induce the enhancement of detector resolution, possibly contributing to discovering new physics. A new technique of pulse shape discrimination will be developed in the future. To apply those methods, storing the waveforms is required, and opening them to the public is recommended.

At the start of plasma operation with deuterium gas in the Large Helical Device (LHD) [48–50], which is classified as a three-dimensional magnetic confinement fusion device characterized by a steady-state operation ability, comprehensive neutron and gamma-ray diagnostics were developed [51]. The typical pulse length of a plasma is 3 s and the maximum neutron flux near the machine is $10^{10} \text{ cm}^{-2} \text{ s}^{-1}$. This is the first deuterium plasma experiment in a large three-dimensional magnetic confinement fusion device. Therefore, advances in energetic particle confinement in three-dimensional magnetic confinement fusion devices were highly expected because neutrons or gamma rays provide information about energetic particles confined inside the plasma. In addition, this is a chance to construct an open-source database of scintillation detector signals in a fusion machine characterized by a steady-state operation ability. After starting the deuterium operation in the LHD, energetic particle confinement research has been intensively performed [52], such as classical confinement of beam ions, confinement of MeV ions, energetic ion distribution measurement, and energetic particle transport due to magnetohydrodynamic instabilities. Our study describes the detailed design and development of a data acquisition system, which is the basis of the neutron and gamma-ray diagnostics for fusion plasma research, and shows the typical measurement result obtained in the LHD.

2. High Sampling Rate Data Acquisition System Working in High Pulse Count Rate Region for Radiation Diagnostics

A high sampling rate data acquisition system providing timestamp, pulse shape information, and waveform, and working in the high pulse count rate region APV8102-14MWPSAGb was developed with Techno AP. The data acquisition system is composed of an analog to digital converter, a field programmable gate array (FPGA), and dynamic random-access memory. The design of the data acquisition board was carried out by Techno AP. Figure 1 shows the block diagram of the data acquisition system.

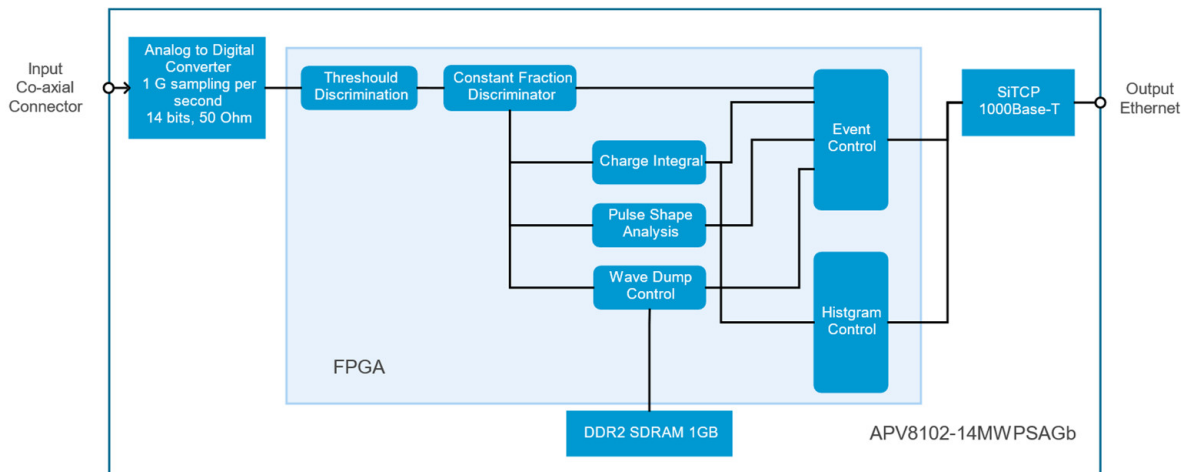


Figure 1. Block diagram of the data acquisition system. The data acquisition system outputs timestamp, pulse shape information, and waveform simultaneously.

A data acquisition board has two channels. An analog to digital converter having 50 Ohm of input impedance and a 14-bit resolution with a 1 GHz sampling rate was chosen because a high bit resolution and a high sampling rate are both important in obtaining superior pulse shape discrimination ability. A 1 GHz sampling rate with a 14-bit resolution creates approximately 2 GB of data per second. A 32 Gbps data transfer rate is used for a board with two channels. For example, in the LHD, for its vertical neutron camera [53], 6 boards were needed. Then, an ~ 200 Gbps average data transfer rate was needed, and 75 GB of data per 3 s, which was the typical LHD discharge period, was stored. A maximum of 200 discharges per day occurred in the LHD, and the stored data needed 15 TB per day. The maximum expected pulse counting rate was 10^6 cps, and the typical pulse width was 30 ns for an organic scintillator. Then, at most $10^6 \text{ s}^{-1} \times 30 \times 10^{-9} \text{ s} = 3\%$ of the data was significant, and 97% of the data was noise. Therefore, we loaded the FPGA and developed a logic circuit to minimize the data required for online and offline waveform analysis. After triggering, the constant fraction discriminator method was implemented to achieve a high resolution with a timestamp of 7.8125 ps. This fine-time resolution is used for time-coincident measurements or time-of-flight measurements [54]. Then, charge integral calculation, pulse shape analysis, and wave dump processing were simultaneously performed. In the charge integral calculation, the total charge of the signal (Q_{total}) was calculated. In the pulse shape analysis, the charge integral of the slow component (Q_{long}) was calculated. For the wave dump, 64 points of the waveform were stored for each trigger. To achieve pulse processing with a high pulse count rate of $\sim 10^6$ cps, the data acquisition system was equipped with 1 GB of synchronous dynamic random-access memory (SDRAM) for each channel. Even though we reduced the data size, $2 \text{ channels} \times 2 \text{ Byte} \times 64 \text{ points} \times 10^6 \text{ s}^{-1}$ caused approximately 2 Gbps. For stable data transfer and data storage, the data were stored on the SDRAM. After finishing data acquisition, the stored data were transferred to the PC via 1000 Base-T ethernet using the SiTCP [55]. The data acquisition board is controlled through the TCP connection. The data acquisition

length was not limited by time but by the number of pulses. The SDRAM could store approximately 4×10^6 pulses.

Details of the data acquisition system are reported in this section. The system acquires the data with 14 bit and 1 GHz sampling. A simultaneous output of timestamp, pulse shape parameter, and waveform, which are required for pulse shape analysis with online and offline modes, were realized by developing the FPGA logic circuit. The system stored four million pulses onto the SDRAM loaded on the board. The data are transferred to a PC after the data acquisition through the 1 Gbps using the TCP connection.

3. Testing of the Data Acquisition System in a Fast Neutron Source

If the one million pulses come in a periodic manner, the time period between the pulses becomes about one microsecond. However, when we consider the radiation measurement, the pulses come randomly. Sometimes a pulse can come right after another pulse, whereas sometimes the time period between them can be more than one microsecond. Therefore, the design of the data acquisition and analysis program becomes complicated and should be tested using the real signal. For the testing of our system, especially for the digital circuit implemented in FPGA, measurement under the high pulse counting rate condition was performed at the accelerator-based deuterium-deuterium (D-D) neutron source in the Fast Neutron Source Facility of the Japan Atomic Energy Agency [56]. Here, a 300 keV, 1 mA deuteron beam was injected into a titanium-deposited copper target. Due to the self-loading of deuterium in the target, D-D neutrons were created with a source D-D neutron rate of $\sim 10^9 \text{ s}^{-1}$. Figure 2 (top) shows the experimental setup of the D-D neutron measurement. A 20 mm diameter and 10 mm height Stilbene scintillator directly coupled with the photomultiplier tube (H11934-100-10MOD, Hamamatsu K.K.) characterized by high gain stability at a high pulse count rate was utilized and loaded on the x -axis manipulator. The output signal was directly connected to the data acquisition system placed next to the irradiation room using a 15 m 50 Ohm double-shield coaxial cable (3D-FB). The data are stored on the PC using the original software after the experiment. The distance between the detector and the target was varied by remote control of the x -axis manipulator to change the D-D neutron flux effectively. The high voltage to the photomultiplier tube was applied by a high voltage module 556, ORTEC. Figure 2 (bottom) shows the typical waveform of scintillation pulses induced by neutrons and gamma rays. The typical pulse width was $\sim 30 \text{ ns}$. The neutron-induced signal has a relatively long decay time compared to the gamma-ray-induced signal.

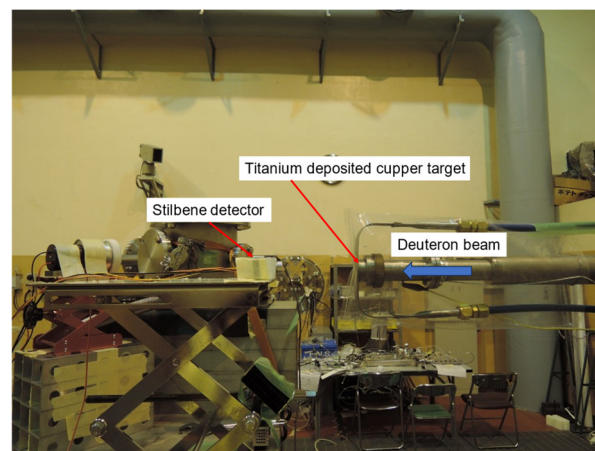


Figure 2. Cont.

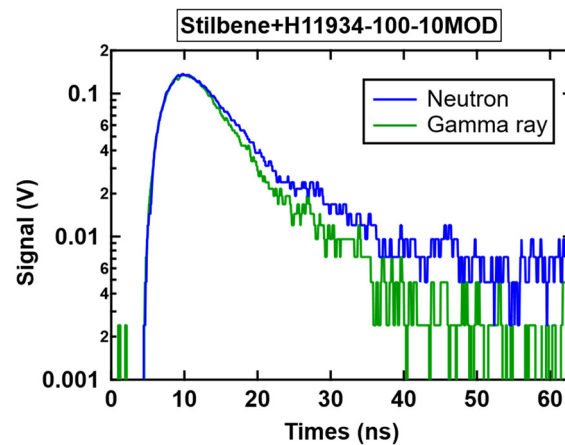


Figure 2. (top) Experimental setup in accelerator-based deuterium-deuterium neutron source (Fast Neutron Source). The Stilbene detector was placed on the front of the deuterium-deuterium neutron source. (bottom) Typical waveform of scintillation pulses. The typical pulse width is 30 ns. The decay time of the neutron and gamma-ray pulses is different.

A test of the data acquisition system was performed under the intense D-D neutron field in the Fast Neutron Source. We changed the distance between the detector and the titanium target from 60 mm to 240 mm, corresponding to 3.5×10^6 to $5.5 \times 10^7 \text{ cm}^{-2}\text{s}^{-1}$ in the D-D neutron flux at the detector position to obtain the relation between neutron flux and the number of pulse signals stored into the data acquisition system. Figure 3 (top) shows the two-dimensional pulse shape discrimination plot obtained under a neutron flux of $5.5 \times 10^7 \text{ cm}^{-2}\text{s}^{-1}$, where the pulse counting rate was 9.4×10^5 count per second (cps). In this experiment, we stored four million pulses in about four seconds. Note that we performed an offline analysis of pulse shape discrimination. Because the decay time of the Stilbene detector signal induced by a neutron is relatively longer than that induced by a gamma ray, we used the charge integral method to discriminate neutron and gamma-ray signals. The longer decay time due to neutron detection induces a relatively high $Q_{\text{long}}/Q_{\text{total}}$. We integrated the signals from 0 ns to 63 ns and from 20 ns to 64 ns for Q_{total} and Q_{long} , respectively. The counts in $Q_{\text{long}}/Q_{\text{total}}$ of ~ 0.15 mainly corresponded to the gamma-ray count, and $Q_{\text{long}}/Q_{\text{total}}$ of ~ 0.2 mainly corresponded to the neutron count. Notably, the pulses in the $Q_{\text{long}}/Q_{\text{total}}$ below 0.1 and above 0.3 were mainly due to the pulse pile-up. The pulse shape discrimination plot showed a high neutron and gamma-ray discrimination ability even at a high pulse count rate. Figure 3 (bottom) shows the pulse count rate as a function of the neutron flux at the detector. The pulse count rate per second monotonically increased with increasing neutron flux at the detector position. Here, live time, i.e., the real time minus the dead time, was considered in the calculation of the pulse count rate. The pulse count rate almost linearly increased with the neutron flux until the pulse count rate was below 6×10^4 cps, and then it deviated from the linear line. Linear fitting up to neutron flux to $3.2 \times 10^7 \text{ cm}^{-2}\text{s}^{-1}$ showed that the pulse count rate was given by the following equation: (pulse count rate) = $0.018 \times (\text{neutron flux } \text{cm}^{-2}) + 54,000$. The pulse count rate of 9.4×10^5 obtained at the neutron flux of $5 \times 10^7 \text{ cm}^{-2}\text{s}^{-1}$ was 10% lower than that of the expected pulse count rate estimated from the linear fitting. The degradation is thought to be mainly due to the processing time of the pulse inside the logic circuit.

The result of the testing of our system in the high pulse count condition is reported in this section. In radiation measurement, the pulse signal comes randomly and the time period between the pulses varies randomly. To check the performance of the developed data acquisition system, we tested the system using the real detector signal at the relatively intense accelerator-based D-D neutron source (Fast Neutron Source). The clear neutron and gamma-ray discrimination shows that the data were stored properly into the board at the pulse counting rate of 900 kcps. It was found that the number of pulses stored into the

board increased with the neutron flux at the detector at the pulse counting rate of 600 kcps, but slightly deviated from 800 kcps. The deviation of the number of stored pulses from the expected value may be caused by the pulse counting loss due to the dead time of the system.

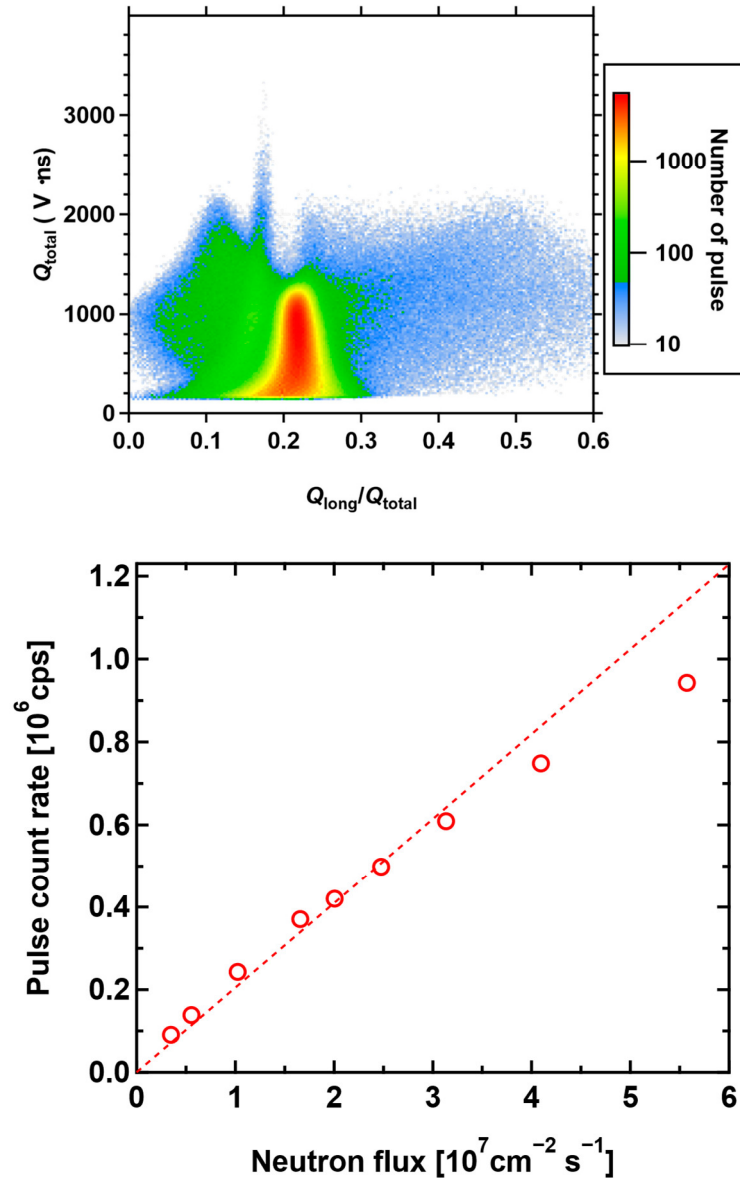


Figure 3. (top) Two-dimensional pulse shape discrimination result under the neutron flux at the detector position of $5.5 \times 10^7 \text{ cm}^{-2} \text{ s}^{-1}$. $Q_{\text{long}}/Q_{\text{total}}$ of ~ 0.15 corresponds to the gamma-ray signal, Whereas $Q_{\text{long}}/Q_{\text{total}}$ of ~ 0.2 corresponds to the neutron signal. The pulses located at $Q_{\text{long}}/Q_{\text{total}}$ above 0.3 are mainly due to the pulse pile-up. Neutron- and gamma ray-induced pulses are clearly separated. (bottom) The pulse count rate as a function of the neutron flux at the detector. The pulse count rate linearly increases with the neutron flux under a pulse count rate of ~ 600 kcps and slightly deviates from 800 kcps.

4. Typical Result in Large Helical Device

4.1. Vertical Neutron Camera for the Radial Profile of the Deuterium-Deuterium Emission Diagnostic

The developed data acquisition system was applied to the vertical neutron camera 1 [57] in the LHD to measure the radial D-D neutron emission profile for the first time in a three-dimensional magnetic confinement fusion device. Figure 4 (top) shows a schematic

drawing of the vertical neutron camera. The vertical neutron camera installed at the base level of the torus hall consists of a multichannel collimator made of heavy concrete and stainless steel tubes, fast neutron scintillation detectors based on the Stilbene scintillator, a photomultiplier tube, and the data acquisition system. The vertical neutron camera 1 has eleven channels that view the plasma from the bottom. The sight lines are placed at the major radius (R) of 3.36 m to 4.26 m with 90 mm steps. Figure 4 (bottom) shows the block diagram of the vertical neutron camera 1. The fast neutron scintillation detector signal is fed into the data acquisition system using a 15 m double-shield coaxial cable. The output data of the data acquisition system are transferred to the PC located outside the torus hall to avoid irradiation effects on the PC [58] by the local network. Then, the data are stored in the LHD data storage [59] and uploaded to the open access server [60]. The high voltage to the photomultiplier tube is applied by the high voltage system APV3304, Techno AP. The voltage value can be adjusted through the ethernet. The latter three dynodes of the photomultiplier tube are connected to the DC voltage power supplies P4K80H and Matsusada Precision to avoid a gain shift of the photomultiplier tube. The DC voltage power supply is controlled through the ethernet via the ethernet controller ET-32 m, Matsusada Precision. The pulse counting rate of the central channel of the vertical neutron camera 1 at the maximum neutron emission rate of the LHD, $5.0 \times 10^{15} \text{ s}^{-1}$, was 600 kcps. The counting loss of the system was negligibly small in the deuterium plasma experiment in the LHD.

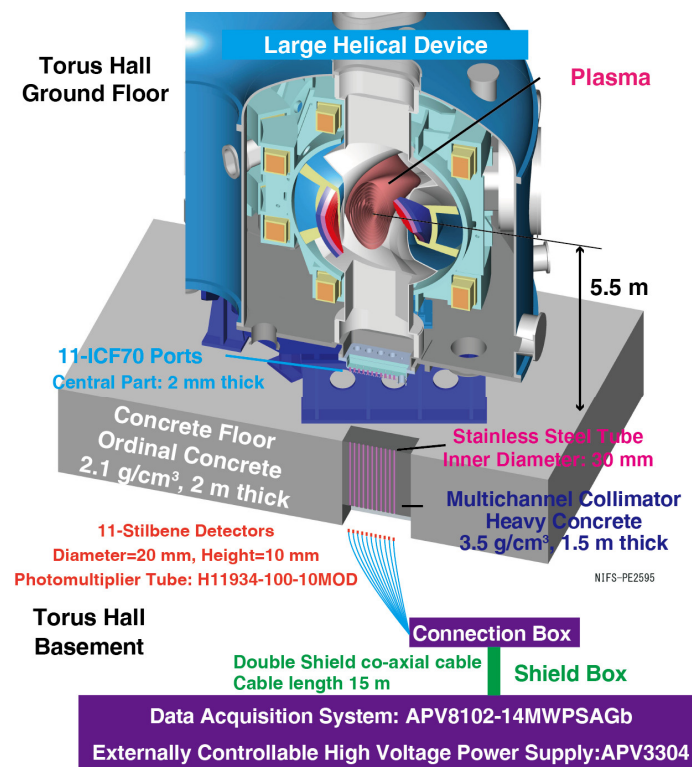


Figure 4. Cont.

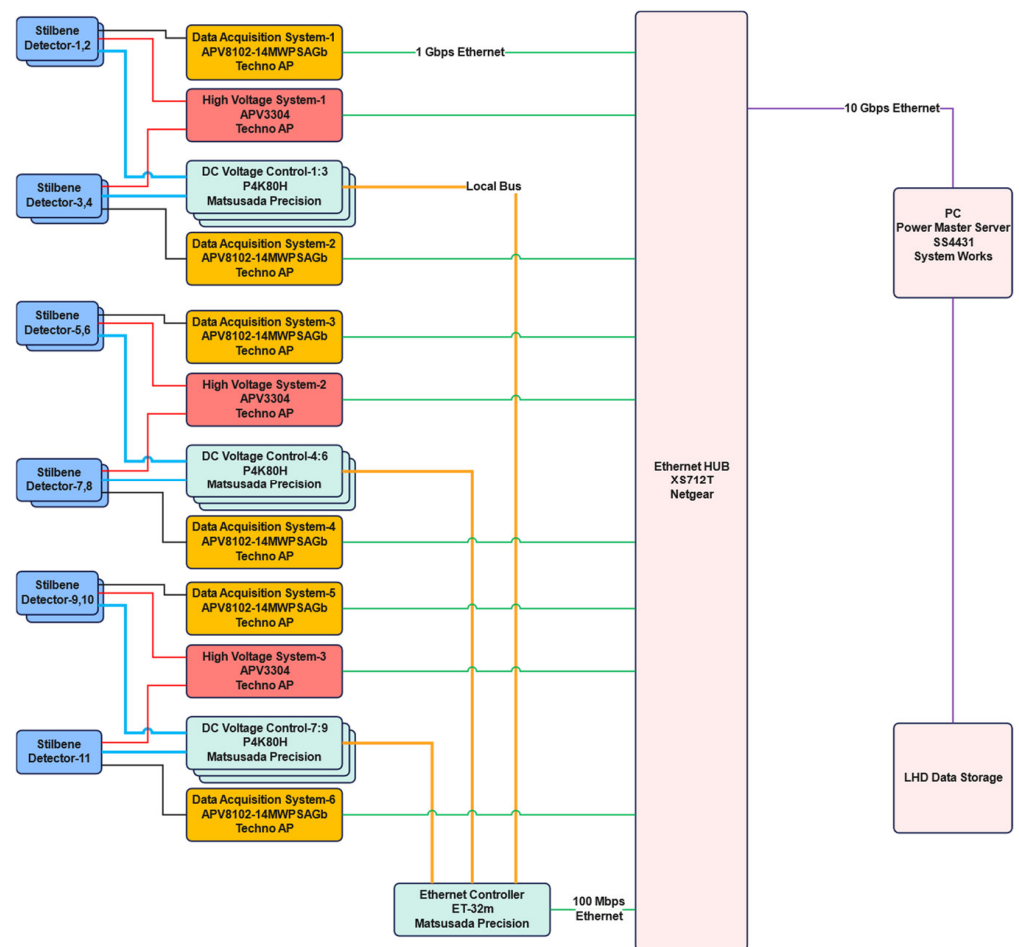


Figure 4. (top) Schematic drawing of the vertical neutron camera 1. The vertical neutron camera mainly consists of a multichannel collimator, 11 Stilbene scintillation detectors, and the data acquisition system. (bottom) Block diagram of the LHD vertical neutron camera.

4.2. Deuterium-Deuterium Neutron Emission Profile Measurement Result

By utilizing the data acquisition system, the neutron emission profile was measured in a perpendicular deuterium-beam-heated deuterium plasma experiment in the LHD. Figure 5 (top) shows the typical time evolution of discharge. The plasma was heated by a perpendicular neutral beam injection (NB5) with an acceleration voltage of 52 keV and an injection power (P_{NB_inj}) of ~ 2 MW. The central electron temperature (T_{e0}) measured by Thomson scattering diagnostics [61] showed that T_{e0} was almost constant at approximately 2 keV. The line-averaged plasma electron density (n_{e_avg}) measured by the far infrared laser interferometer [62] showed that n_{e_avg} was slightly increased from $1 \times 10^{19} \text{ m}^{-3}$ to $1.8 \times 10^{19} \text{ m}^{-3}$. The total neutron emission rate (S_n) measured by the neutron flux monitor [63] showed that S_n increased from $2 \times 10^{13} \text{ s}^{-1}$ to $3 \times 10^{13} \text{ s}^{-1}$. The time evolution of the neutron count measured by the vertical neutron camera 1 showed that the neutron count per 100 ms was at most ~ 100 , and the peak neutron count existed at an R of 3.72 m to 3.81 m. We compared the obtained line-integrated neutron emission profile at t of 6.0 s to 7.0 s with that by a numerical calculation based on the experiment data. In the numerical calculation, the three-dimensional equilibrium was reconstructed using the VMEC2000 code [64]. The birth profile of beam ions was calculated using the HFREYA module of the FIT3D code [65]. The beam ion distribution function at the vertical neutron camera 1 cross section was calculated by the guiding center orbit-following models in the Boozer coordinates DELTA5D [66]. By the beam ion distribution function, D-D neutron emission rate was calculated based on the beam-thermal reaction reactivity [67] using D-D cross section [68]. Figure 5 (bottom left) shows the neutron emissivity profile

calculated by the numerical simulation. The numerical simulation predicted that there is a relatively high neutron emissivity region at $Z \sim -0.6$ m and an R of 3.6 to 3.9 m. The poloidal structure was formed because the perpendicular deuterium beam mainly created helically trapped ions that were trapped in the helical ripple formed by the twisted twin coils [69]. Figure 5 (bottom right) shows the comparison of the line-integrated neutron emission profile obtained in the experiment and calculated by the numerical simulation. The calculated line-integrated neutron emission profile qualitatively agreed with the experimental results. By utilizing our developed data acquisition system, the visualization of the radial profile of helically trapped ions was successful for the first time. The data acquisition system worked steadily during the deuterium operation of the LHD for six years.

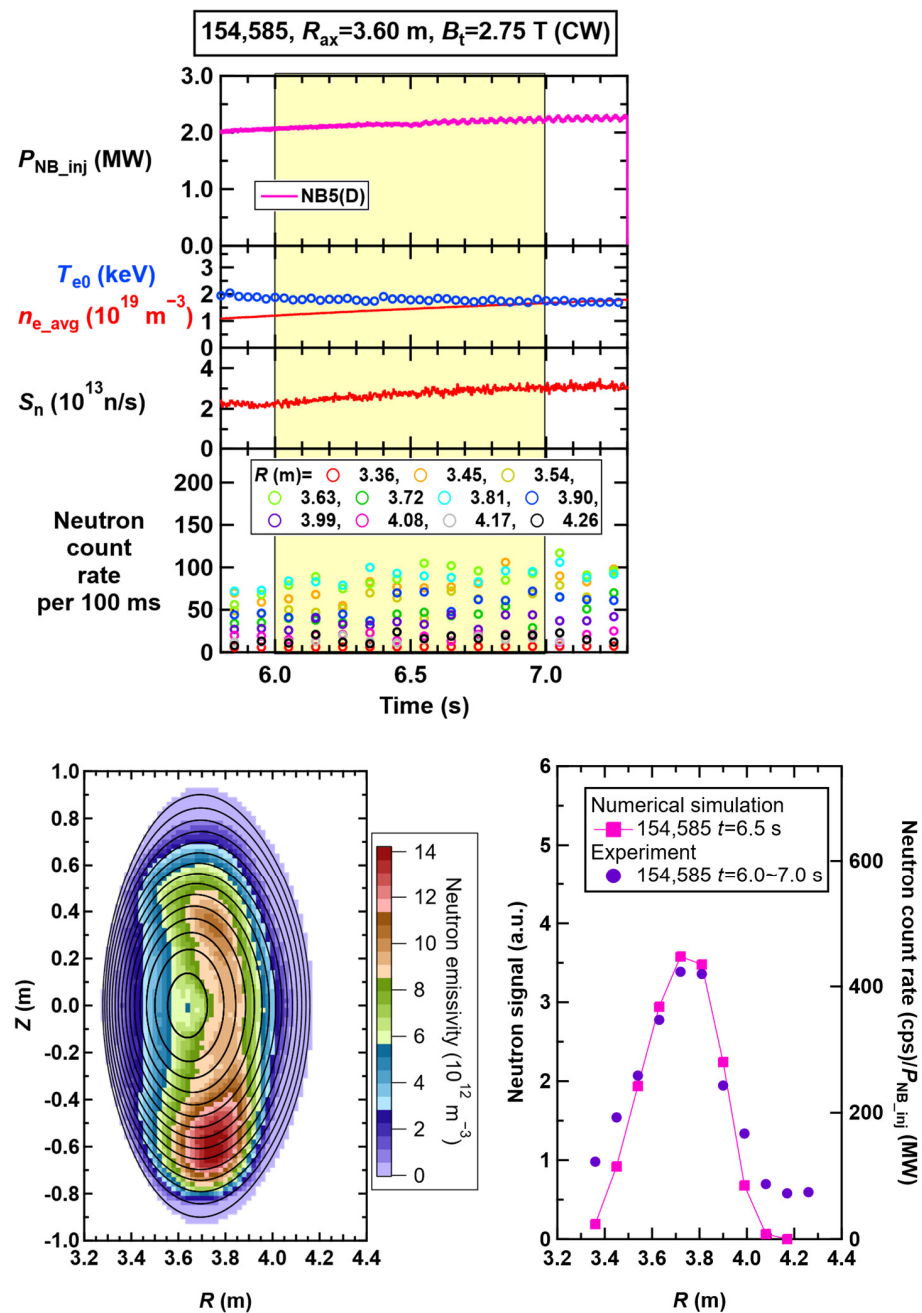


Figure 5. (top) Typical waveform of perpendicular deuterium-injected deuterium discharge in the LHD. (bottom left) Two-dimensional D-D neutron emissivity calculated based on the beam ion orbit-following model. (bottom right) Comparison of line-integrated neutron emission profiles obtained in an experiment and predicted by a numerical simulation.

In this section, the result of neutron diagnostics based on the developed data acquisition system in the LHD is reported. The high counting rate stability of the system enabled us to obtain the line-integrated neutron profile in the maximum neutron emission discharge of the LHD, at an S_n of $5 \times 10^{15} \text{ s}^{-1}$. The experimentally obtained radial profile of neutron emission was compared with that obtained by numerical simulation based on the orbit-following models using the experimental data. The experimentally obtained neutron emission profile was consistent with that predicted by the numerical simulations. By using the data acquisition system, the first visualization of the radial density profile of helically trapped beam ions was realized.

5. Discussion

The data acquisition system has worked for deuterium plasma discharge in the LHD without any serious trouble for six years. The stored data were uploaded on the open access server. The long-time stability of the data acquisition system should be continuously checked. The maximum counting rate of the detector at the central channel of vertical neutron camera 1 in the LHD was 600 kcps, and the high counting capability of the system was enough for LHD measurement. In future, the logic system implemented into the FPGA could be rearranged to achieve a higher counting rate operation. The data acquisition system will be applied to the radial neutron camera for the JAERI Tokamak-60 super advanced experiment [70]. Also, the developed system can be used for general radiation diagnostics. Therefore, applications to accelerators, e.g., Linear International Fusion Materials Irradiation Facility Prototype Accelerator [71,72] and Japan Proton Accelerator Research Complex [73], as well as medical applications, e.g., Boron Neutron Capture Therapy [74–76], will be expected.

6. Summary

A high counting resistance, high time resolution data acquisition system simultaneously providing the timestamp, pulse shape information, and waveform, was developed for radiation diagnostics in magnetic confinement fusion plasma research. The data acquisition was composed of a 14-bit 1 GHz fast analog to digital convertor, a field programmable gate array, and a 1 GB synchronous dynamic random access memory. Testing of the data acquisition system under a high counting rate condition was performed in the accelerator-based intense deuterium-deuterium neutron source (Fast Neutron Source). The pulse count acquired by the system almost linearly increased below ~800 kcps, showing that the system works properly below ~800 kcps. The developed data acquisition system was used with a vertical neutron camera 1 to measure the deuterium-deuterium neutron emission profile in the LHD. The data acquisition system operated stably without severe counting loss in the deuterium operation of the LHD from 2017 to 2022. The qualitative agreement of the neutron emission profile obtained in the experiment and the prediction by numerical simulation based on the orbit-following models using experimental data shows that this was the first measurement of the radial D-D neutron emission profile in a three-dimensional magnetic confinement fusion device. The data, i.e., timestamp, pulse shape parameter based on the charge integral method, and waveform, are now stored in an open access server. The data will be one of the standard waveforms of scintillation signal in magnetic confinement fusion machines. Applications of radiation measurement in other fields such as accelerators and medical research are desired.

Author Contributions: Conceptualization, K.O. and M.I.; methodology, K.O. and M.I.; software, K.O.; validation, K.O., S.S. and L.Y.L.; formal analysis, K.O.; investigation, S.S. and L.Y.L.; resources, K.O.; data curation, K.O., M.I. and E.T.; writing—original draft preparation, K.O.; writing—review and editing, M.I. and E.T.; visualization, K.O.; supervision, M.I.; project administration, M.I.; funding acquisition, M.I. All authors have read and agreed to the published version of the manuscript.

Funding: This research received no external funding.

Data Availability Statement: The data supporting the findings of this study are available in the LHD experiment data repository at <https://doi.org/10.57451/lhd.analyzed-data> (accessed on 13 September 2023).

Acknowledgments: We are pleased to acknowledge the assistance of Techno AP, the FNS Experiment Group, and the LHD Experiment Group.

Conflicts of Interest: The authors declare no conflict of interest.

References

1. Ongena, J.; Koch, R.; Wolf, R.; Zohm, H. Magnetic-confinement fusion. *Nat. Phys.* **2016**, *12*, 398–410. [[CrossRef](#)]
2. Pearson, R.J.; Costley, A.E.; Phaal, R.; Nuttall, W.J. Technology Roadmapping for mission-led agile hardware development: A case study of a commercial fusion energy start-up. *Technol. Forecast. Soc. Chang.* **2020**, *158*, 120064. [[CrossRef](#)]
3. Young, K.M. An Assessment of the Penetrations in the First Wall Required for Plasma Measurements for Control of an Advanced Tokamak Plasma Demo. *Fusion Sci. Technol.* **2017**, *57*, 298–304. [[CrossRef](#)]
4. Orsitto, F.P.; Villari, R.; Moro, F.; Todd, T.N.; Lilley, S.; Jenkins, I.; Felton, R.; Biel, W.; Silva, A.; Scholz, M.; et al. Diagnostics and control for the steady state and pulsed tokamak DEMO. *Nucl. Fusion* **2016**, *56*, 026009. [[CrossRef](#)]
5. Biel, W.; de Baar, M.; Dinklage, A.; Felici, F.; Konig, R.; Meister, H.; Treutterer, W.; Wenninger, R. DEMO diagnostics and burn control. *Fusion Eng. Des.* **2015**, *96–97*, 8–15. [[CrossRef](#)]
6. Fasoli, A.; Gormenzano, C.; Berk, H.L.; Breizman, B.; Briguglio, S.; Darrow, D.S.; Gorelenkov, N.; Heidbrink, W.W.; Jaun, A.; Konovalov, S.V.; et al. Chapter 5: Physics of energetic ions. *Nucl. Fusion* **2007**, *47*, S264–S284. [[CrossRef](#)]
7. Gorelenkov, N.N.; Pinches, S.D.; Toi, K. Energetic particle physics in fusion research in preparation for burning plasma experiments. *Nucl. Fusion* **2014**, *54*, 125001. [[CrossRef](#)]
8. Heidbrink, W.W.; Sadler, G.J. The Behavior of Fast Ions in Tokamak Experiments. *Nucl. Fusion* **1994**, *34*, 535–615. [[CrossRef](#)]
9. Jarvis, O.N. Neutron Measurement Techniques for Tokamak Plasmas. *Plasma Phys. Control. Fusion* **1994**, *36*, 209–244. [[CrossRef](#)]
10. Osakabe, M.; Takeiri, Y.; Morisaki, T.; Motojima, G.; Ogawa, K.; Isobe, M.; Tanaka, M.; Murakami, S.; Shimizu, A.; Nagaoka, K.; et al. Current Status of Large Helical Device and Its Prospect for Deuterium Experiment. *Fusion Sci. Technol.* **2017**, *72*, 199–210. [[CrossRef](#)]
11. Kiptily, V.G.; Cecil, F.E.; Medley, S.S. Gamma ray diagnostics of high temperature magnetically confined fusion plasmas. *Plasma Phys. Control. Fusion* **2006**, *48*, R59–R82. [[CrossRef](#)]
12. Medley, S.S.; Scott, S.D.; Roquemore, A.L.; Cecil, F.E. Performance of the fusion gamma diagnostic on TFTR. *Rev. Sci. Instrum.* **1990**, *61*, 3226–3228. [[CrossRef](#)]
13. Cecil, F.E.; Liu, H.; Scorby, J.C.; Medley, S.S. Prompt gamma ray diagnostics of advanced fuel fusion plasmas. *Rev. Sci. Instrum.* **1990**, *61*, 3223–3225. [[CrossRef](#)]
14. Cecil, F.E.; Medley, S.S. Gamma ray measurements during deuterium and ^3He discharges on TFTR. *Nucl. Instrum. Methods Phys. Res. Sect. A Accel. Spectrom. Detect. Assoc. Equip.* **1988**, *271*, 628–635. [[CrossRef](#)]
15. Magee, R.M.; Ogawa, K.; Tajima, T.; Allfrey, I.; Gota, H.; McCarroll, P.; Ohdachi, S.; Isobe, M.; Kamio, S.; Klumper, V.; et al. First measurements of p11B fusion in a magnetically confined plasma. *Nat. Commun.* **2023**, *14*, 955. [[CrossRef](#)] [[PubMed](#)]
16. Cheng, C.Z.; Chance, M.S. Low-n shear Alfvén spectra in axisymmetric toroidal plasmas. *Phys. Fluids* **1986**, *29*, 3695. [[CrossRef](#)]
17. Chen, L. Theory of magnetohydrodynamic instabilities excited by energetic particles in tokamaks. *Phys. Plasmas* **1994**, *1*, 1519–1522. [[CrossRef](#)]
18. Kiptily, V.G.; Fitzgerald, M.; Goloborodko, V.; Sharapov, S.E.; Challis, C.D.; Frigione, D.; Graves, J.; Mantsinen, M.J.; Beaumont, P.; Garcia-Munoz, M.; et al. Fusion product losses due to fishbone instabilities in deuterium JET plasmas. *Nucl. Fusion* **2018**, *58*, 014003. [[CrossRef](#)]
19. Heidbrink, W.W.; Strait, E.J.; Doyle, E.; Sager, G.; Snider, R.T. An Investigation of Beam Driven Alfvén Instabilities in the DIII-D Tokamak. *Nucl. Fusion* **1991**, *31*, 1635–1648. [[CrossRef](#)]
20. Toi, K.; Ogawa, K.; Isobe, M.; Osakabe, M.; Spong, D.A.; Todo, Y. Energetic-ion-driven global instabilities in stellarator/helical plasmas and comparison with tokamak plasmas. *Plasma Phys. Control. Fusion* **2011**, *53*, 024008. [[CrossRef](#)]
21. Duong, H.H.; Heidbrink, W.W.; Strait, E.J.; Petrie, T.W.; Lee, R.; Moyer, R.A.; Watkins, J.G. Loss of Energetic Beam Ions during TAE Instabilities. *Nucl. Fusion* **1993**, *33*, 749–765. [[CrossRef](#)]
22. Darrow, D.S.; Zweben, S.J.; Chang, Z.; Cheng, C.Z.; Diesso, M.D.; Fredrickson, E.D.; Mazzucato, E.; Nazikian, R.; Phillips, C.K.; Popovichev, S.; et al. Observations of neutral beam and ICRF tail ion losses due to Alfvén modes in TFTR. *Nucl. Fusion* **1997**, *37*, 939–954. [[CrossRef](#)]
23. Giacomelli, L.; Zimbal, A.; Tittelmeier, K.; Schuhmacher, H.; Tardini, G.; Neu, R.; Team, A.U. The compact neutron spectrometer at ASDEX Upgrade. *Rev. Sci. Instrum.* **2011**, *82*, 123504. [[CrossRef](#)] [[PubMed](#)]
24. Rigamonti, D.; Zhong, G.Q.; Croci, G.; Giacomelli, L.; Gorini, G.; Hu, Z.; Muraro, A.; Nocente, M.; Perelli Cippo, E.; Rebai, M.; et al. First neutron spectroscopy measurements with a compact C7LYC based detector at EAST. *J. Instrum.* **2019**, *14*, C09025. [[CrossRef](#)]

25. Binda, F.; Eriksson, J.; Ericsson, G.; Hellesen, C.; Conroy, S.; Nocente, M.; Sundén, E.A. Generation of the neutron response function of an NE213 scintillator for fusion applications. *Nucl. Instrum. Methods Phys. Res. Sect. A Accel. Spectrom. Detect. Assoc. Equip.* **2017**, *866*, 222–229. [CrossRef]
26. Iwanowska, J.; Swiderski, L.; Krakowski, T.; Moszynski, M.; Szczesniak, T.; Pausch, G. The time-of-flight method for characterizing the neutron response of liquid organic scintillators. *Nucl. Instrum. Methods Phys. Res. Sect. A Accel. Spectrom. Detect. Assoc. Equip.* **2015**, *781*, 44–49. [CrossRef]
27. Yuan, X.; Zhang, X.; Xie, X.; Gorini, G.; Chen, Z.; Peng, X.; Chen, J.; Zhang, G.; Fan, T.; Zhong, G.; et al. Neutron energy spectrum measurements with a compact liquid scintillation detector on EAST. *J. Instrum.* **2013**, *8*, P07016. [CrossRef]
28. Adams, J.M.; Jarvis, O.N.; Sadler, G.J.; Syme, D.B.; Watkins, N. The JET neutron emission profile monitor. *Nucl. Instrum. Methods Phys. Res. Sect. A: Accel. Spectrom. Detect. Assoc. Equip.* **1993**, *329*, 277–290. [CrossRef]
29. Ishikawa, M.; Nishitani, T.; Kusama, Y.; Sukegawa, A.; Takechi, M.; Shinohara, K.; Krasilnikov, A.; Kashuck, Y.; Sasao, M.; Isobe, M.; et al. Neutron Emission Profile Measurement and Fast Charge Exchange Neutral Particle Flux Measurement for Transport Analysis of Energetic Ions in JT-60U. *Plasma Fusion Res.* **2007**, *2*, 019. [CrossRef]
30. Esposito, B.; Marocco, D.; Gandolfo, G.; Belli, F.; Bertalot, L.; Blocki, J.; Bocian, D.; Brolatti, G.; Cecconello, M.; Centioli, C.; et al. Progress of Design and Development for the ITER Radial Neutron Camera. *J. Fusion Energy* **2022**, *41*, 22. [CrossRef]
31. Zhong, G.Q.; Hu, L.Q.; Pu, N.; Zhou, R.J.; Xiao, M.; Cao, H.R.; Zhu, Y.B.; Li, K.; Fan, T.S.; Peng, X.Y.; et al. Status of neutron diagnostics on the experimental advanced superconducting tokamak. *Rev. Sci. Instrum.* **2016**, *87*, 11D820. [CrossRef]
32. Cui, Z.Q.; Xie, X.F.; Tong, J.J.; Qu, J.Y.; Hu, Z.M. Design of a neutron camera for the HL-2A tokamak. *Nucl. Instrum. Methods Phys. Res. Sect. A Accel. Spectrom. Detect. Assoc. Equip.* **2019**, *942*, 162332. [CrossRef]
33. Uchida, Y.; Takada, E.; Fujisaki, A.; Isobe, M.; Ogawa, K.; Shinohara, K.; Tomita, H.; Kawarabayashi, J.; Iguchi, T. A study on fast digital discrimination of neutron and gamma-ray for improvement neutron emission profile measurement. *Rev. Sci. Instrum.* **2014**, *85*, 11E118. [CrossRef] [PubMed]
34. Riva, M.; Esposito, B.; Marocco, D.; Belli, F.; Syme, B.; Contributors, J.-E. The new digital electronics for the JET Neutron Profile Monitor: Performances and first experimental results. *Fusion Eng. Des.* **2011**, *86*, 1191–1195. [CrossRef]
35. Cester, D.; Lunardon, M.; Nebbia, G.; Stevanato, L.; Viesti, G.; Petrucci, S.; Tintori, C. Pulse shape discrimination with fast digitizers. *Nucl. Instrum. Methods Phys. Res. Sect. A Accel. Spectrom. Detect. Assoc. Equip.* **2014**, *748*, 33–38. [CrossRef]
36. CAEN. Available online: <https://www.caen.it/> (accessed on 13 September 2023).
37. DPP-PSD. Available online: <https://www.caen.it/products/dpp-psd/> (accessed on 13 September 2023).
38. Perkins, L.J.; Scott, M.C. The application of pulse shape discrimination in NE 213 to neutron spectrometry. *Nucl. Instrum. Methods* **1979**, *166*, 451–464. [CrossRef]
39. Phillips, G.W.; Marlow, K.W. Automatic analysis of gamma-ray spectra from germanium detectors. *Nucl. Instrum. Methods* **1976**, *137*, 525–536. [CrossRef]
40. Firk, F.W.K. Neutron time-of-flight spectrometers. *Nucl. Instrum. Methods* **1979**, *162*, 539–563. [CrossRef]
41. Winyard, R.A.; Lutkin, J.E.; McBeth, G.W. Pulse shape discrimination in inorganic and organic scintillators. I. *Nucl. Instrum. Methods* **1971**, *95*, 141–153. [CrossRef]
42. D'Mellow, B.; Aspinall, M.D.; Mackin, R.O.; Joyce, M.J.; Peyton, A.J. Digital discrimination of neutrons and -rays in liquid scintillators using pulse gradient analysis. *Nucl. Instrum. Methods Phys. Res. Sect. A Accel. Spectrom. Detect. Assoc. Equip.* **2007**, *578*, 191–197. [CrossRef]
43. McBeth, G.W.; Lutkin, J.E.; Winyard, R.A. A simple zero crossing pulse shape discrimination system. *Nucl. Instrum. Methods* **1971**, *93*, 99–102. [CrossRef]
44. Yousefi, S.; Lucchese, L.; Aspinall, M.D. Digital discrimination of neutrons and gamma-rays in liquid scintillators using wavelets. *Nucl. Instrum. Methods Phys. Res. Sect. A Accel. Spectrom. Detect. Assoc. Equip.* **2009**, *598*, 549–553. [CrossRef]
45. Flores, J.L.; Martel, I.; Jiménez, R.; Galán, J.; Salmerón, P. Application of neural networks to digital pulse shape analysis for an array of silicon strip detectors. *Nucl. Instrum. Methods Phys. Res. Sect. A Accel. Spectrom. Detect. Assoc. Equip.* **2016**, *830*, 287–293. [CrossRef]
46. Griffiths, J.; Kleinegesse, S.; Saunders, D.; Taylor, R.; Vacheret, A. Pulse shape discrimination and exploration of scintillation signals using convolutional neural networks. *Mach. Learn. Sci. Technol.* **2020**, *1*, 045022. [CrossRef]
47. Fu, C.; Di Fulvio, A.; Clarke, S.D.; Wentzloff, D.; Pozzi, S.A.; Kim, H.S. Artificial neural network algorithms for pulse shape discrimination and recovery of piled-up pulses in organic scintillators. *Ann. Nucl. Energy* **2018**, *120*, 410–421. [CrossRef]
48. Takeiri, Y. The Large Helical Device: Entering Deuterium Experiment Phase Toward Steady-State Helical Fusion Reactor Based on Achievements in Hydrogen Experiment Phase. *IEEE Trans. Plasma Sci.* **2018**, *46*, 2348–2353. [CrossRef]
49. Takeiri, Y. Prospect Toward Steady-State Helical Fusion Reactor Based on Progress of LHD Project Entering the Deuterium Experiment Phase. *IEEE Trans. Plasma Sci.* **2018**, *46*, 1141–1148. [CrossRef]
50. Takeiri, Y. Advanced Helical Plasma Research towards a Steady-State Fusion Reactor by Deuterium Experiments in Large Helical Device. *Atoms* **2018**, *6*, 69. [CrossRef]
51. Isobe, M.; Ogawa, K.; Nishitani, T.; Miyake, H.; Kobuchi, T.; Pu, N.; Kawase, H.; Takada, E.; Tanaka, T.; Li, S.Y.; et al. Neutron Diagnostics in the Large Helical Device. *IEEE Trans. Plasma Sci.* **2018**, *46*, 2050–2058. [CrossRef]

52. Ogawa, K.; Isobe, M.; Nishitani, T.; Murakami, S.; Seki, R.; Nuga, H.; Kamio, S.; Fujiwara, Y.; Yamaguchi, H.; Saito, Y.; et al. Energetic ion confinement studies using comprehensive neutron diagnostics in the Large Helical Device. *Nucl. Fusion* **2019**, *59*, 076017. [CrossRef]
53. Ogawa, K.; Isobe, M.; Osakabe, M. Progress on Integrated Neutron Diagnostics for Deuterium Plasma Experiments and Energetic Particle Confinement Studies in the Large Helical Device During the Campaigns from FY2017 to FY2019. *Plasma Fusion Res.* **2021**, *16*, 1102023. [CrossRef]
54. Zhang, Y.; Ge, L.; Hu, Z.; Sun, J.; Li, X.; Ogawa, K.; Isobe, M.; Sangaroon, S.; Liao, L.; Yang, D.; et al. Design and optimization of an advanced time-of-flight neutron spectrometer for deuterium plasmas of the large helical device. *Rev. Sci. Instrum.* **2021**, *92*, 053547. [CrossRef] [PubMed]
55. SiTCP. Available online: <https://rd.kek.jp/project/soi/SEABAS/> (accessed on 13 September 2023).
56. IAEA TECDOC SERIES. *Compendium of Neutron Beam Facilities for High Precision Nuclear Data Measurements*; International Atomic Energy Agency, Vienna International Centre: Vienna, Austria, 2014.
57. Ogawa, K.; Isobe, M.; Nishitani, T.; Kobuchi, T. The large helical device vertical neutron camera operating in the MHz counting rate range. *Rev. Sci. Instrum.* **2018**, *89*, 113509. [CrossRef] [PubMed]
58. Ogawa, K.; Nishitani, T.; Isobe, M.; Murata, I.; Hatano, Y.; Matsuyama, S.; Nakanishi, H.; Mukai, K.; Sato, M.; Yokota, M.; et al. Investigation of irradiation effects on highly integrated leading-edge electronic components of diagnostics and control systems for LHD deuterium operation. *Nucl. Fusion* **2017**, *57*, 086012. [CrossRef]
59. Nakanishi, H.; Ohsuna, M.; Kojima, M.; Imazu, S.; Nonomura, M.; Hasegawa, M.; Nakamura, K.; Higashijima, A.; Yoshikawa, M.; Emoto, M.; et al. Data Acquisition and Management System of LHD. *Fusion Sci. Technol.* **2010**, *58*, 445–457. [CrossRef]
60. Open_Access_Server. Available online: <https://w3-ext.lhd.nifs.ac.jp/dx/lhd.vnc25.xxxxx> (accessed on 13 September 2023).
61. Yamada, I.; Narihara, K.; Funaba, H.; Minami, T.; Hayashi, H.; Kohmoto, T. Recent Progress of the LHD Thomson Scattering System. *Fusion Sci. Technol.* **2017**, *58*, 345–351. [CrossRef]
62. Akiyama, T.; Kawahata, K.; Tanaka, K.; Tokuzawa, T.; Ito, Y.; Okajima, S.; Nakayama, K.; Michael, C.A.; Vyacheslavov, L.N.; Sanin, A.; et al. Interferometer Systems on Lhd. *Fusion Sci. Technol.* **2010**, *58*, 352–363. [CrossRef]
63. Ito, D.; Yazawa, H.; Tomitaka, M.; Kumagai, T.; Kono, S.; Yamauchi, M.; Misawa, T.; Kobuchi, T.; Hayashi, H.; Miyake, H.; et al. Development of a Wide Dynamic Range Neutron Flux Measurement Instrument Having Fast Time Response for Fusion Experiments. *Plasma Fusion Res.* **2021**, *16*, 1405018. [CrossRef]
64. Hirshman, S.P.; Betancourt, O. Preconditioned Descent Algorithm for Rapid Calculations of Magnetohydrodynamic Equilibria. *J. Comput. Phys.* **1991**, *96*, 99–109. [CrossRef]
65. Murakami, S.; Nakajima, N.; Okamoto, M. Finite β Effects on the ICRF and NBI Heating in the Large Helical Device. *Fusion Technol.* **1995**, *27*, 256–259. [CrossRef]
66. Spong, D.A. Three-dimensional effects on energetic particle confinement and stability. *Phys. Plasmas* **2011**, *18*, 056109. [CrossRef]
67. Mikkelsen, D.R. Approximation for non-resonant beam target fusion reactivities. *Nucl. Fusion* **1989**, *29*, 1113–1115. [CrossRef]
68. Bosch, H.S.; Hale, G.M. Improved Formulas for Fusion Cross-Sections and Thermal Reactivities. *Nucl. Fusion* **1992**, *32*, 611–631. [CrossRef]
69. Murakami, S.; Wakasa, A.; Maaßberg, H.; Beidler, C.D.; Yamada, H.; Watanabe, K.Y.; LHD Experimental Group. Neoclassical transport optimization of LHD. *Nucl. Fusion* **2002**, *42*, L19–L22. [CrossRef]
70. Sumida, S.; Shinohara, K.; Nishitani, T.; Ogawa, K.; Bando, T.; Sukegawa, A.M.; Ishikawa, M.; Takada, E.; Bierwage, A.; Oyama, N. Conceptual design of a collimator for the neutron emission profile monitor in JT-60SA using Monte Carlo simulations. *Rev. Sci. Instrum.* **2020**, *91*, 113504. [CrossRef]
71. Kondo, K.; Akagi, T.; Arranz, F.; Bazin, N.; Bellan, L.; Bolzon, B.; Brañas, B.; Cara, P.; Carin, Y.; Castellanos, J.; et al. Validation of the Linear IFMIF Prototype Accelerator (LIPAc) in Rokkasho. *Fusion Eng. Des.* **2020**, *153*, 111503. [CrossRef]
72. Dzitko, H.; Cara, P.; Carin, Y.; Chel, S.; Facco, A.; Gex, D.; Hasegawa, K.; Kasugai, A.; Kondo, K.; Massaut, V.; et al. Status and future developments of the Linear IFMIF Prototype Accelerator (LIPAc). *Fusion Eng. Des.* **2021**, *168*, 112621. [CrossRef]
73. Hotchi, H.; Kinsho, M.; Hasegawa, K.; Hayashi, N.; Hikichi, Y.; Hiroki, S.; Kamiya, J.; Kanazawa, K.; Kawase, M.; Noda, F.; et al. Beam commissioning of the 3-GeV rapid cycling synchrotron of the Japan Proton Accelerator Research Complex. *Phys. Rev. Spec. Top.—Accel. Beams* **2009**, *12*, 040402. [CrossRef]
74. Moss, R.L. Critical review, with an optimistic outlook, on Boron Neutron Capture Therapy (BNCT). *Appl. Radiat. Isot.* **2014**, *88*, 2–11. [CrossRef]
75. Dymova, M.A.; Taskaev, S.Y.; Richter, V.A.; Kuligina, E.V. Boron neutron capture therapy: Current status and future perspectives. *Cancer Commun.* **2020**, *40*, 406–421. [CrossRef]
76. Ichikawa, G.; Tsuchida, K.; Kiyonagi, Y.; Ishikawa, A.; Hirata, Y.; Yoshihashi, S.; Watanabe, K.; Uritani, A.; Hamano, T.; Ogawara, R.; et al. Development of thermal neutron moderator for testing boron agents for Boron Neutron Capture Therapy (BNCT). *J. Instrum.* **2019**, *14*, T06010. [CrossRef]

Disclaimer/Publisher’s Note: The statements, opinions and data contained in all publications are solely those of the individual author(s) and contributor(s) and not of MDPI and/or the editor(s). MDPI and/or the editor(s) disclaim responsibility for any injury to people or property resulting from any ideas, methods, instructions or products referred to in the content.